*Physica* **48** (1970) 13–42 © *North-Holland Publishing Co.*

# INELASTIC NEUTRON SCATTERING INVESTIGATION OF SPIN WAVES AND MAGNETIC INTERACTIONS IN $Cr_2O_3$ †

E. J. SAMUELSEN‡, M. T. HUTCHINGS and G. SHIRANE
*Brookhaven National Laboratory, Upton, New York, USA*

Received 24 October 1969

**Synopsis**

The dispersion relation $E(\boldsymbol{q})$ for spin waves in $Cr_2O_3$ has been measured at 78 K by means of inelastic neutron scattering using a triple-axis spectrometer. The spin-wave energy is found to vary between 7.9 K (0.68 meV) at the Brillouin zone centre to 635 K (54.7 meV) at the zone boundary near (111). The data were fitted to a theoretical $E(\boldsymbol{q})$ derived from a Heisenberg Hamiltonian involving neighbours out to about 6.1 Å distance. It is found that the interactions to the first and second neighbours are strong, but weak interactions exist out to at least the fifth neighbours (4.1 Å). The sublattice magnetization, the Néel point, the Curie–Weiss temperature and the perpendicular susceptibility are calculated using the spin-wave data and are found to agree well with observations. The density of spin-wave states is also calculated.

1. *Introduction.* Chromium sesquioxide, $Cr_2O_3$, is an antiferromagnetic material which has received considerable attention during recent years. It has the relatively complicated corundum ($\alpha$–$Al_2O_3$) structure and is chemically isomorphous with $\alpha$–$Fe_2O_3$ which also shows interesting antiferromagnetic properties. After it had been established in 1953 that the spin structure of $Cr_2O_3$ below its Néel point ($T_N$ = 308 K) differs[1]) from that of $\alpha$–$Fe_2O_3$, the question arose as to the reason for the difference. The answer was naturally sought in the different electronic configuration of the $Cr^{3+}$ and the $Fe^{3+}$ ions, which could give rise to quite different exchange or superexchange interactions between the near neighbours[2,3]). Many attempts have been made to predict the relative strengths of the various pair interactions in the two compounds along these lines[2–6]). In retrospect, the work by Goodenough[4]) in 1960 is probably the one that gave predictions for $Cr_2O_3$ in best qualitative agreement with the present measurements.

Work on the $Cr_2O_3$–$\alpha$–$Fe_2O_3$ solid solution is here of some interest. Li[2]) in 1956 from his estimates of the exchange interactions in the two compounds,

† Work performed under the auspices of the U. S. Atomic Energy Commision.

‡ Guest scientist on leave from Institutt for Atomenergi, Kjeller, Norway.

tried to picture the magnetic phase diagram of the system. Experimentally, the system was studied by magnetic and neutron-diffraction measurements by Cox *et al.*[7]) in 1962. It was found that the spin structures of the end members of the solid solution merely represent special cases of a more general spin structure, namely cone spirals found in a wide composition range. The stability criteria in terms of the relative interaction strengths for the various configurations were subsequently worked out by Bertaut[8]). However, although interesting in themselves, these studies furnished no firm conclusion on the strength of the interactions in the two compounds.

An important step towards an understanding of the magnetic properties of $Cr_2O_3$ was taken in 1963 when Foner[9]) published his antiferromagnetic resonance (AFMR) and susceptibility data. The rather unusual temperature dependence he observed for the AFMR frequency has later been interpreted by Anderson and Callen[10]) as due to the phase boundary between the antiferromagnetic and the spin-flop state. The magnitude of the uniaxial anisotropy field has been reinterpreted in later work by Foner and his coworkers[11]). Foner's observation that the parallel susceptibility does not reach zero at $T = 0$ was explained by Silverstein and Jacobs[12]) as due to a Van Vleck temperature-independent term.

Spectroscopists have long been interested in the connection between the magnetic interactions and the occurrence of splitting of the red R-lines in $Cr_2O_3$[13–14]), but information on the interaction strenghts has not been obtained from these studies. The same R-lines are known to occur in the laser material ruby ($\alpha$–$Al_2O_3$ with small amounts of $Cr_2O_3$), which also shows a multitude of weaker satellite lines now interpreted as arising from exchange-coupled $Cr^{3+}$ pairs[15–16]). Mollenauer and Schawlow, in a careful piezospectroscopic study[15]), were able to attribute a great many of the lines to the four nearest-neighbour pairs and to find the strength of the interactions from line intensities versus temperature. Although their values are of great interest as a comparison with $Cr_2O_3$, we show in the present work that the interactions in $Cr_2O_3$ are different from those in ruby. Paramagnetic resonance studies of ruby[17]) have also furnished some information on these pair interactions.

Restricted neutron scattering studies of spin waves in $Cr_2O_3$ have previously been reported. Samuelsen[18]) has measured the low-energy part of the dispersion relation, and Alikhanov *et al.* in a very recent publication[19]) have estimated the values of the four nearest-neighbour interactions. Samuelsen[20]) has also measured the variation with temperature of the energy of long-wavelength spin waves and shown that it follows the sublattice magnetization quite closely.

The present study was undertaken to measure the full spin-wave dispersion relation and derive the exchange-interaction constants. Short accounts of the work have already appeared[21]).

2. *The experiments.* 2.1. Sample and instrument. The sample used in the measurements was a single crystal of approximately cylindrical shape, 0.7 cm in diameter and 1.8 cm in length (0.7 $cm^3$ volume). It was prepared by the Verneuil technique and contains less than 0.015% impurities of Al, Si, Cu, Ca, Mg, Mn and Fe. The sample is the same crystal as used for the investigation of the spin-wave energy versus temperature[20]).

The crystal was mounted in a frame of thin aluminum, which in turn was attached to the coldfinger of a liquid nitrogen dewar. The temperature was kept constant at (78 $\pm$ 0.5) K throughout the measurements.

The measurements were performed on a triple-axis spectrometer at the HFBR reactor. Germanium monochromator and analyser crystals were used. The (111) reflections were utilised for incident energies 13 meV and 24.6 meV and the (311) reflections for energies 50, 70 and 90 meV. (We shall use 1 meV = 11.60 K = 8.066 $cm^{-1}$ as the energy unit whenever we discuss neutron measurements. Spin-wave energies and exchange interactions are given in K). In the beam path (fig. 1) were inserted Soller slit collimators of horizontal divergence $\alpha_0 = 0.35°$, $\alpha_1 = 0.7°$, $\alpha_2 = 0.7°$, and $\alpha_3 = 0.35°$. Occasionally tighter collimation was used. The effective vertical divergency was about 2.5°.

When working with an incident beam of energy 13 meV, a 2.5 cm thick

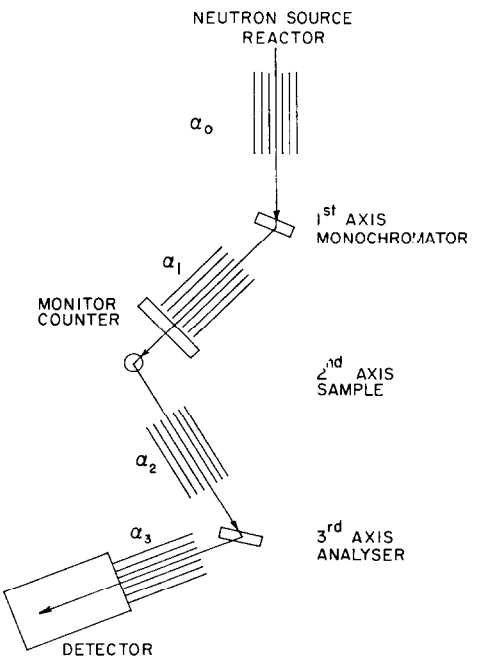


Fig. 1. Sketch of the beam path in a neutron triple-axis spectrometer. The Soller slit collimators, with horizontal openings $\alpha_i$, are indicated.

pyrolytic graphite filter was inserted in the beam before the monitor counter to reduce the higher-order contamination of the beam. Second-order scattering ($13 \cdot 2^2$ meV) is unimportant from Ge (111) because it can only occur via multiple-scattering processes since the structure factor for (222) is zero. Some contribution from third order ($13 \cdot 3^2$ meV) was found to be reduced by 91%, while the 13 meV intensity itself was reduced by 43% by the filter.

2.2. The measurements. The single crystal of $Cr_2O_3$ was mounted in the cryostat on the spectrometer table with its rhombohedral $[1\bar{1}0]$ zone axis vertical, so that the spin waves observed were all confined to the $(1\bar{1}0)^*$ plane. There are three equivalent $(1\bar{1}0)^*$ planes intersecting along the [111] axis, which is contained in the plane of scattering. A thorough exploration of the spin waves in one $(1\bar{1}0)^*$ plane gives in fact a very large amount of the information contained in the entire Brillouin zone, as equivalent planes will be only $\pm 60°$ apart (rotated around [111]).

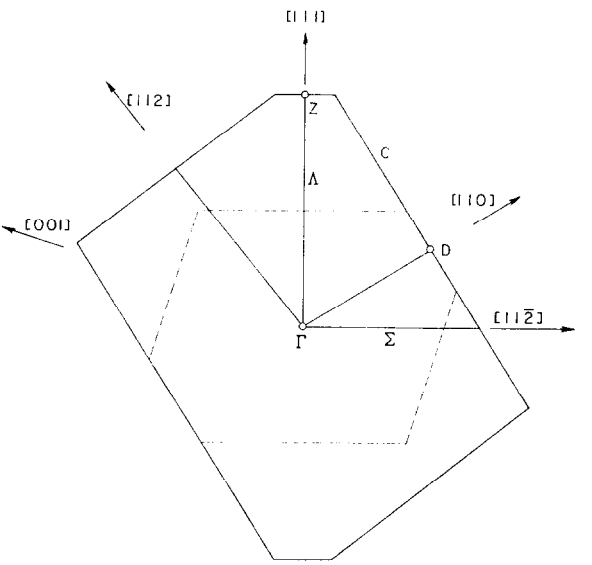


Fig. 2. The Brillouin zone (B.Z.) in the rhombohedral $(1\bar{1}0)^*$ plane of the $Cr_2O_3$ spin structure. The dashed line shows the B.Z. for the chemical structure.

The Brillouin zone in the $(1\bar{1}0)^*$ plane for the magnetic structure of $Cr_2O_3$ is shown in fig. 2. Also shown by dashed lines is the Brillouin zone (B.Z.) for the $\alpha$–$Fe_2O_3$ spin structure, which coincides with the B.Z. of the chemical corundum structure. The larger magnetic B.Z. for $Cr_2O_3$ reflects the fact that for the magnetic ions alone, a unit cell containing only two $Cr^{3+}$ ions may be chosen[22]), whereas the chemical cell contains four.

The antiferromagnetic structure of $Cr_2O_3$ below $T_N = 308$ K is such that no purely magnetic reflections exist. The ones with largest magnetic structure factors are (110), (002), (112), (222), and (220)[1]), and these are also the ones around which spin-wave scattering will occur with highest intensity[22]). Most of the present measurements were performed at (110) which contains most magnetic contribution at 78 K, but some measurements at (222) were found necessary because of focussing requirements.

Within the zone shown in fig. 2, spin waves were observed from the zone centre $\Gamma$ to the zone boundaries in the [112], [111], [110], and [112] directions, as well as along the zone boundary line C. Some measurements were also made in an arbitrary direction near [112].

3. *Resolution correction for the triple-axis spectrometer.* 3.1. Triple-axis spectrometer. A triple-axis spectrometer (fig. 1) is an instrument for measuring the simultaneous momentum ($\hbar\boldsymbol{Q}$) and energy ($\hbar\omega$) transfer between a neutron beam and a crystal sample. The monochromating crystal is placed on the first axis so as to determine the momentum ($\hbar\boldsymbol{k}_0$) and energy ($E_0 = (\hbar^2/2m_0)\, k_0^2$) of the beam incident on the sample, placed on the second axis. The scattered beam from the sample, having a wave vector $\boldsymbol{k}$, is energy analysed ($E = (\hbar^2/2m_0)\, k^2$) by means of Bragg reflection from the analyser crystal on the third axis. ($m_0$ is the neutron mass.)

Conservation of energy and momentum requires that

$$E - E_0 = \hbar\omega \tag{1}$$

and

$$\hbar(\boldsymbol{k} - \boldsymbol{k}_0) = \hbar\boldsymbol{Q}. \tag{2}$$

If an excitation (spin wave) of wave vector $\boldsymbol{q}$ has been created in the scattering process, then

$$\boldsymbol{Q} = \boldsymbol{\tau} + \boldsymbol{q}, \tag{3}$$

where $\boldsymbol{\tau}$ is some reciprocal lattice vector. In its "constant $Q$" mode, the instrument is set for a predetermined momentum transfer $\hbar\boldsymbol{Q}$ while $\hbar\omega$ is changed stepwise in such a way that eqs. (1) and (2) are simultaneously obeyed. If some excitation of wave vector $\boldsymbol{q} = \boldsymbol{Q} - \boldsymbol{\tau}$ takes place, a peak in the scattered intensity would be seen at an $\hbar\omega$ corresponding to the energy of the excitation, $E(\boldsymbol{q})$. In a "constant $E$" experiment, $\hbar\omega$ is kept fixed and $Q$ is varied.

The present measurements were usually performed with the "constant $Q$" technique, although some "constant $E$" runs were made at isolated points.

3.2. Resolution function. Due to the finite spread of the energies and momenta of the incident and scattered neutron beam, neutrons of other momentum and energy transfers than the desired $\hbar\boldsymbol{Q}$ and $\hbar\omega$ will also be de-

tected. The resolution function $R(\Delta\boldsymbol{Q}, \hbar\Delta\omega)$ of the instrument measures the probability of detecting scattering due to momentum and energy transfers $\hbar\boldsymbol{Q} = \hbar(\boldsymbol{Q}_0 + \Delta\boldsymbol{Q})$ and $\hbar\omega = \hbar\omega_0 + \hbar\Delta\omega$, respectively, when the instrument is set to measure $\hbar\boldsymbol{Q}_0$ and $\hbar\omega_0$. Among the various papers on the resolution properties of the triple-axis spectrometer, the treatment given recently by Cooper and Nathans[23]) is particularly comprehensive. Assuming Gaussian forms of the mosaic spread of the monochromator and analyser crystals and approximating the triangular openings of the collimator-slit systems to Gaussians, they derive a Gaussian form for $R(\Delta\boldsymbol{Q}, \hbar\Delta\omega)$:

$$R(\Delta\boldsymbol{Q}, \hbar\Delta\omega) \sim \exp - \tfrac{1}{2} \sum_{i,j}^{4} M_{ij} \cdot X_i \cdot X_j. \tag{4}$$

$X_i$ are the Cartesian components along chosen $X$, $Y$, and $Z$ axes of $\Delta\boldsymbol{Q}$ for $i = 1, 2, 3$, respectively, and $X_4 = \hbar\Delta\omega$. Cooper and Nathans[23]) developed the explicit expressions for the matrix elements $M_{ij}$ in terms of the spectrometer parameters (collimation and mosaic spread) and incident and outgoing beam momenta and energies. Contours of constant value of the $R$-function as given by eq. (4) are seen to constitute ellipsoids in the four-dimensional $X_i$ space. The concept of such resolution ellipsoids is very useful in understanding and predicting the best experimental conditions for a given measurement. Further the relatively simple form of eq. (4) makes the mathematical treatment of the resolution tractable. Eq. (4) has proved to give a surprisingly close description of the properties of the triple-axis spectrometer[24]), and the present work furnishes additional support to its applicability.

3.3. Peak shape and position. The resolution function $R(\Delta\boldsymbol{Q}, \hbar\Delta\omega)$ is a property of the instrument and contains no reference to the properties of the scattering sample. It is derived[23]) by considering the probabilities for neutrons to pass the various devices (monochromator and analyser crystals, collimators) along the beam path, and then integrating over all combinations of $\boldsymbol{k}_0$ and $\boldsymbol{k}$ that conserve the momentum transfer to $\hbar(\boldsymbol{Q}_0 + \Delta\boldsymbol{Q})$ and the energy transfer to $\hbar(\omega_0 + \Delta\omega)$. If the intensity $\sigma'(\Delta\boldsymbol{Q}, \hbar\Delta\omega)$ is required instead, the cross section for scattering by the sample from $\boldsymbol{k}_0$ to $\boldsymbol{k}$ and the sensitivity of the detector system must be invoked before the integration is performed. It is found that $\sigma'(\Delta\boldsymbol{Q}, \hbar\Delta\omega)$ contains $R(\Delta\boldsymbol{Q}, \hbar\Delta\omega)$ as a factor. It will furthermore contain the properties of the sample through the Bose population factor, the dynamical structure factor and the energy and momentum $\delta$ functions, $\delta(\hbar\omega \mp E(\boldsymbol{q})) \cdot \delta(\boldsymbol{Q} - \boldsymbol{\tau} \mp \boldsymbol{q})$. To obtain the observable intensity $I(\boldsymbol{Q}_0, \hbar\omega_0)$, $\sigma'(\Delta\boldsymbol{Q}, \hbar\Delta\omega)$ has to be integrated over all $\Delta\boldsymbol{Q}$ and $\hbar\Delta\omega$, a four-dimensional integration in $X_i$. The $X_4$-integration may be performed using the energy $\delta$-function, and the

remaining three-dimensional integration may be performed numerically on a computer.

We have derived the general expressions for $\sigma'(\Delta \boldsymbol{Q}, \hbar\Delta\omega)$ and have written a program to calculate the peak profiles $I(\boldsymbol{Q}_0, \hbar\omega_0)$, usually expressed as functions of $\hbar\omega_0$ for constant $\boldsymbol{Q}_0$. The dynamical structure factor and the energy dispersion relation $E(\boldsymbol{q})$ must be known for the scattering system, but the program is otherwise kept general.

Theoretical expressions for the dynamical structure factor and $E(\boldsymbol{q})$ for spin waves in $Cr_2O_3$ have been derived by Samuelsen[22]). Preliminary values of the exchange parameters involved were obtained by fitting $E(\boldsymbol{q})$ to the uncorrected experimental energy versus wave vector data. The $E(\boldsymbol{q})$ was then used to calculate the peak shape $I(\boldsymbol{Q}_0, \hbar\omega_0)$ and the peak position for specified $\boldsymbol{q} = \boldsymbol{Q}_0 - \boldsymbol{\tau}$, from which an indication of the necessary correction was found. Fig. 3 and 4 show some observed and calculated peak profiles. The $E(\boldsymbol{q})$ used for the calculated peaks is the best fit to the corrected data using five parameters (next section). The arrows indicate the nominal spin-wave energy for which the calculations were made.

It is to be noticed that the peak shapes are very well reproduced by the calculations, indicating that the resolution folding procedure used is sufficiently accurate. It is further seen that the location of the peak maxima are often shifted considerably with respect to the corresponding $E(\boldsymbol{q})$. This

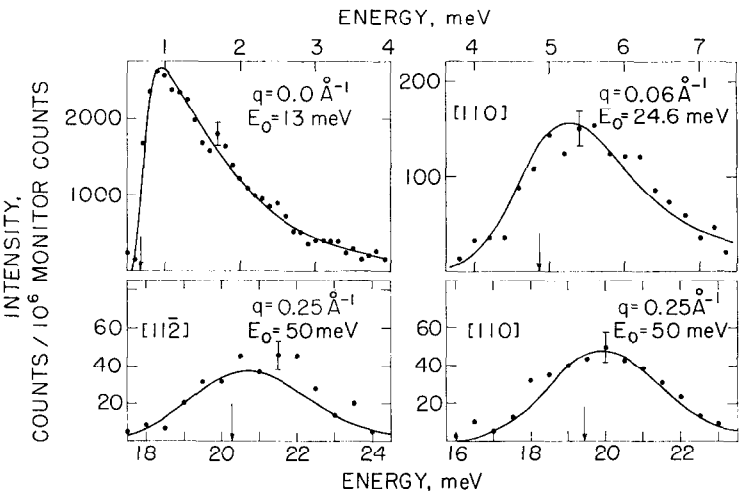


Fig. 3. Examples of observed and calculated neutron-scattering peak profiles in energy scans of the triple-axis spectrometer. Lengths and directions of the spin-wave wave vector $\boldsymbol{q}$ are shown for each case, as well as incident neutron energy $E_0$. The calculated curves for $E_0 = 13$ and 24.6 meV have been individually normalised to the measurements at one point. For $E_0 = 50$ meV only the right-hand curve is normalised. The arrows indicate the nominal spin-wave energy $E(\boldsymbol{q})$. The observed points are corrected for background.

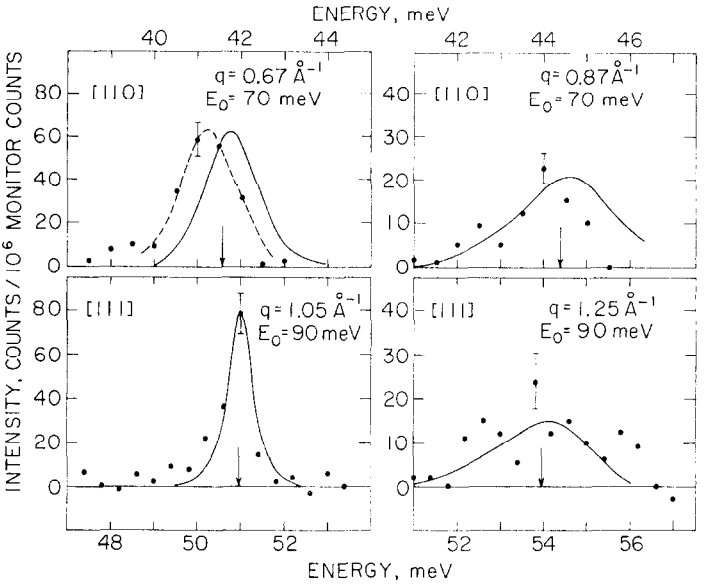


Fig. 4. Observed and calculated neutron scattering peak profiles showing focussed and non-focussed peaks. Only one of the two calculated peaks for each incident energy is normalised to the measurements. The arrows indicate the nominal spin-wave energy $E(\boldsymbol{q})$. The observed points are corrected for background.

shift is of course entirely an instrumental effect, and indicates the magnitude of the required correction of the experimental energy values. It was found that most of the shift is due to the finite vertical collimation used in the experiments. The correction is largest in the low-energy region of $E(\boldsymbol{q})$. Thus for $\boldsymbol{q} = 0$, the peak is shifted about 30% to higher energies. This particular point is a good check of the calculations as the spin-wave energy is known to be 0.68 meV from AFMR by Foner[9]). Fig. 3 shows that the experimental peak shape is well reproduced, and that the neutron data are in fact compatible with the AFMR data. For high energies, near the Z.B. the energy shift is quite small (fig. 4).

The shift varies with the degree of "focussing" attained in a particular measurement. Because of the rather steep slope of $E$ versus $\boldsymbol{q}$ in the linear part of the dispersion relation for $Cr_2O_3$, good focussing was never attained there. However, in a limited region of $\boldsymbol{q}$ one could find that the inclination of the resolution ellipsoid happens to coincide with the slope of $E(\boldsymbol{q})$, producing very narrow peaks, which turned out to be practically unshifted by instrumental effects of the type being discussed (fig. 4). It is known[23]) that the resolution ellipsoid is inclined in $\omega$–$\mathbf{Q}$-space and extended in the direction near that of the outgoing neutron beam. Referring to that direction

as the "transverse" direction, the shift was found to be smallest for "transverse" $\boldsymbol{q}$ and largest for "longitudinal" $\boldsymbol{q}$ (normal to "transverse").

4. *Spin-wave dispersion relation and exchange parameters.* The unit cell and the atomic arrangement of the corundum lattice is shown in fig. 5, and the exchange interaction parameters $J_m$ for neighbours out to the 12th in $Cr_2O_3$ are identified in table I. The spin-wave dispersion relation $E(\boldsymbol{q})$ has been given previously[22]). Assuming a Heisenberg Hamiltonian of the form

$$\mathscr{H} = - \sum_{nn',\, jj'} J_{nn'jj'} \cdot \boldsymbol{S}_{nj} \cdot \boldsymbol{S}_{n'j'} - \mu_B \cdot \sum_{nj} g_{nj} \cdot H_{A_{nj}} \cdot S^z_{nj}, \tag{5}$$

it was shown that $E(\boldsymbol{q})$ is of the form

$$E(\boldsymbol{q}) = [(A + C)^2 - (BB^* + DD^* + BD^* + B^*D)]^{\frac{1}{2}}. \tag{6}$$

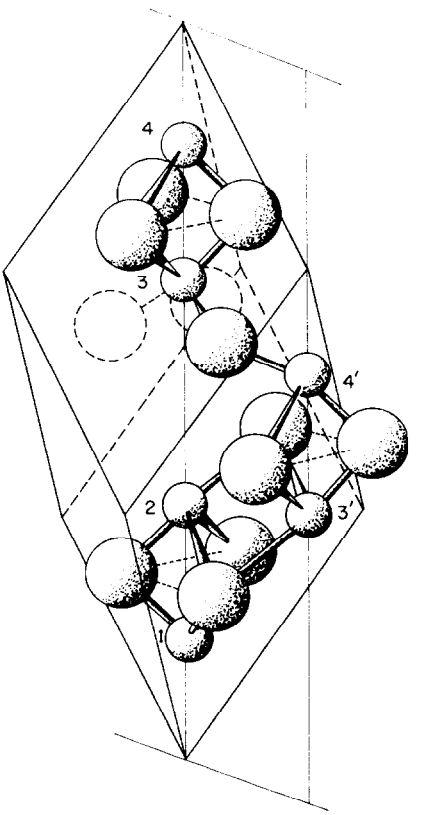


Fig. 5. The rhombohedral unit cell of the corundum structure, showing some details of the ionic arrangements. Small balls: metal ions. Large balls: oxygen ions. The correspondence between metal ion pairs and some of the exchange interaction constants is indicated in table I.

TABLE 1

Identification of the twelve nearest-neighbour exchange interactions $J_m$ in $Cr_2O_3$. $\boldsymbol{t}_i$ is any of the three rhombohedral lattice vectors, $\boldsymbol{Z} = \boldsymbol{t}_1 + \boldsymbol{t}_2 + \boldsymbol{t}_3$, and $\rho_{12}\cdot\boldsymbol{Z}$ is the smallest Cr–Cr distance along [111]. The numbers in the "spin(ion) pair" column refer to the enumeration of fig. 5.

| Exchange interaction $J_m$ | Spin(ion) pair | Number of neighbours | Cr–Cr distance (Å) | Interatomic vectors |
|---|---|---|---|---|
| $J_1$ | + − (1–2) | 1 | 2.65 | $\rho_{12}\cdot\boldsymbol{Z}$ |
| $J_2$ | + − (2–3′) | 3 | 2.89 | $\boldsymbol{t}_i - (\frac{1}{2} - \rho_{12})\cdot\boldsymbol{Z}$ |
| $J_3$ | + − (3–4′) | 3 | 3.43 | $\rho_{12}\cdot\boldsymbol{Z} - \boldsymbol{t}_i$ |
| $J_4$ | + + (2–4′) | 6 | 3.65 | $\pm(\boldsymbol{Z}/2 - \boldsymbol{t}_i)$ |
| $J_5$ | + − (2–3) | 1 | 4.1 | $-(\frac{1}{2} - \rho_{12})\cdot\boldsymbol{Z}$ |
| $J_6$ | + + | 6 | 5.0 | $\pm(\boldsymbol{t}_i - \boldsymbol{t}_j),\ i \neq j$ |
| $J_7$ | + + (4′–4) | 6 | 5.4 | $\pm\,\boldsymbol{t}_i$ |
| $J_8$ | + − | 6 | 5.6 | $\pm(\boldsymbol{t}_i - \boldsymbol{t}_j) + \rho_{12}\cdot\boldsymbol{Z},\ i \neq j$ |
| $J_9$ | + − (1–4′) | 3 | 5.7 | $(\frac{1}{2} + \rho_{12})\cdot\boldsymbol{Z} - \boldsymbol{t}_i$ |
| $J_{10}$ | + − | 3 | 5.8 | $(\frac{1}{2} + \rho_{12})\cdot\boldsymbol{Z} - 2\boldsymbol{t}_i$ |
| $J_{11}$ | + − | 3 | 6.0 | $2\boldsymbol{t}_i - (1 - \rho_{12})\,\boldsymbol{Z}$ |
| $J_{12}$ | + + | 6 | 6.1 | $\pm(2\boldsymbol{t}_i - \boldsymbol{Z}/2)$ |

Expressions for $A$, $B$, $C$, $D$ were given[22] for the case of four near-neighbour interactions $J_{nn'jj'} = J_m$, $m = 1$ to 4, and an effective anisotropy field $H_A$. During the processing of our experimental spin-wave data, we found it necessary to extend the analysis beyond this limit. We give the expressions for $A$, $BB^*$, $C$, $DD^*$ and $BD^* + B^*D$ in appendix I, including interactions out to the 12th nearest neighbours.

The experimentally determined spin-wave dispersion relation (after corrections have been applied for instrumental resolution) is tabulated in table II and most of it is shown graphically in fig. 6. The energy at the zone centre $\Gamma(\boldsymbol{q} = 0)$ is taken from Foner's more accurate AFMR data[9]. The linear part of $E(\boldsymbol{q})$ in the [110] direction is compared with previous "diffraction technique" measurements[20] in fig. 7, and excellent agreement is found. In the linear region a quantity $\Delta$ is defined[22] as a measure of the deviation from directional isotropy of $E(\boldsymbol{q})$, ($\Delta = 0$ for isotropic $E(\boldsymbol{q})$). Using the slopes of the dispersion relation in the [111] and [11$\bar{2}$] directions, we find $\Delta = -0.28 \pm 0.08$, which is a much more accurate value than $-0.15 \pm 0.24$ found by the diffraction technique[20].

The experimentally measured dispersion relation was fitted to the theoretical $E(\boldsymbol{q})$ of eq. (6) by means of a computer program using a least-squares fitting routine written by Powell[25]. The program minimized the following

TABLE II

Observed and calculated spin-wave energies for $Cr_2O_3$ at 78 K. The spin-wave propagation directions [*hkl*] refer to the rhombohedral lattice. The experimental conditions are specified by the incident neutron energy $E_0$(*m*eV), the lattice point at which measurements are performed ((222) and (110)) and the spectrometer configuration (W and AW). The energy for $q = 0.0$ is taken from AFMR[9]. Calculated energies are shown for various numbers $N$ of fitted parameters, with reference to table III.

| Direction [*hkl*] | Experimental condition | $q$ (Å$^{-1}$) | $E_{obs}$ (meV) | $\Delta E$ (meV) | $E_{calc}$(meV) $N=2$ | $N=4$ | $N=5$ | $N=10$ | $N=12$ |
|---|---|---|---|---|---|---|---|---|---|
| | | 0.0 | 0.68 | — | 0.68 | 0.68 | 0.68 | 0.68 | 0.68 |
| [111] | 13 | 0.01 | 1.05 | 0.1 | 0.93 | 0.97 | 0.98 | 0.99 | 1.08 |
| | (222) | 0.02 | 1.80 | 0.2 | 1.43 | 1.53 | 1.56 | 1.58 | 1.64 |
| | W | 0.03 | 2.25 | 0.3 | 2.01 | 2.17 | 2.22 | 2.25 | 2.29 |
| | | 0.04 | 3.00 | 0.3 | 2.61 | 2.83 | 2.90 | 2.94 | 2.97 |
| | | 0.05 | 3.90 | 0.4 | 3.22 | 3.50 | 3.59 | 3.64 | 3.66 |
| | | 0.06 | 4.45 | 0.4 | 3.84 | 4.17 | 4.29 | 4.34 | 4.35 |
| | 24.6 | 0.04 | 2.85 | 0.4 | 2.61 | 2.83 | 2.90 | 2.94 | 2.97 |
| | (110) | 0.05 | 3.70 | 0.4 | 3.22 | 3.50 | 3.59 | 3.64 | 3.66 |
| | W | 0.06 | 4.20 | 0.5 | 3.84 | 4.17 | 4.29 | 4.34 | 4.35 |
| | 50 | 0.05 | 3.6 | 0.9 | 3.22 | 3.50 | 3.59 | 3.64 | 3.66 |
| | (110) | 0.08 | 6.1 | 0.9 | 5.08 | 5.52 | 5.68 | 5.75 | 5.75 |
| | AW | 0.10 | 7.3 | 0.9 | 6.33 | 6.88 | 7.06 | 7.16 | 7.16 |
| | | 0.11 | 8.2 | 0.8 | 6.95 | 7.55 | 7.76 | 7.86 | 7.86 |
| | | 0.14 | 10.0 | 0.8 | 8.82 | 9.57 | 9.83 | 9.95 | 9.94 |
| | | 0.15 | 10.4 | 0.8 | 9.44 | 10.24 | 10.51 | 10.64 | 10.63 |
| | | 0.17 | 12.3 | 0.8 | 10.67 | 11.57 | 11.87 | 12.01 | 12.00 |
| | | 0.20 | 14.5 | 1.0 | 12.52 | 13.56 | 13.89 | 14.04 | 14.02 |
| | | 0.21 | 15.1 | 0.5 | 13.13 | 14.22 | 14.55 | 14.71 | 14.69 |
| | | 0.23 | 16.5 | 1.0 | 14.35 | 15.52 | 15.87 | 16.03 | 16.01 |
| | | 0.26 | 18.4 | 1.0 | 16.17 | 17.45 | 17.81 | 17.98 | 17.95 |
| | W | 0.10 | 6.0 | 0.8 | 6.33 | 6.88 | 7.06 | 7.16 | 7.16 |
| | | 0.15 | 10.2 | 0.5 | 9.44 | 10.24 | 10.51 | 10.64 | 10.63 |
| | | 0.18 | 12.3 | 0.5 | 11.29 | 12.24 | 12.54 | 12.69 | 12.67 |
| | | 0.21 | 14.5 | 0.5 | 13.13 | 14.22 | 14.55 | 14.71 | 14.69 |
| | 70 | 0.31 | 21.0 | 1.0 | 19.16 | 20.60 | 20.95 | 21.13 | 21.10 |
| | (110) | 0.46 | 29.8 | 0.6 | 27.72 | 29.40 | 29.55 | 29.68 | 29.65 |
| | W | 0.53 | 33.3 | 0.8 | 31.45 | 33.10 | 33.11 | 33.19 | 33.18 |
| | | 0.63 | 37.5 | 0.4 | 36.44 | 37.88 | 37.67 | 37.70 | 37.68 |
| | | 0.68 | 39.8 | 0.4 | 38.76 | 40.04 | 39.74 | 39.74 | 39.73 |
| | | 0.75 | 42.8 | 0.5 | 41.81 | 42.79 | 42.39 | 42.37 | 42.37 |

TABLE II (*continued*)

| Direction [*hkl*] | Experimental condition | $q$ (Å$^{-1}$) | $E_{obs}$ (meV) | $\Delta E$ (meV) | $E_{calc}$(meV) $N=2$ | $N=4$ | $N=5$ | $N=10$ | $N=12$ |
|---|---|---|---|---|---|---|---|---|---|
| | 90 | 0.75 | 42.2 | 0.5 | 41.81 | 42.79 | 42.39 | 42.37 | 42.37 |
| | (110) | 0.85 | 45.7 | 0.4 | 45.69 | 46.16 | 45.74 | 45.71 | 45.72 |
| | W | 0.95 | 48.5 | 0.3 | 48.99 | 48.89 | 48.59 | 48.57 | 48.58 |
| | | 1.05 | 51.0 | 0.3 | 51.66 | 51.00 | 50.94 | 50.94 | 50.94 |
| | | 1.15 | 52.9 | 0.4 | 53.67 | 52.53 | 52.74 | 52.75 | 52.75 |
| | | 1.25 | 53.8 | 0.7 | 55.00 | 53.51 | 53.95 | 53.98 | 53.98 |
| | | 1.38 | 53.7 | 1.2 | 55.66 | 53.99 | 54.58 | 54.60 | 54.60 |
| [110] | 13 | 0.005 | .95 | 0.2 | 0.79 | 0.79 | 0.79 | 0.79 | 0.90 |
| | (110) | 0.01 | 1.20 | 0.2 | 1.05 | 1.05 | 1.05 | 1.06 | 1.15 |
| | W | 0.015 | 1.45 | 0.3 | 1.38 | 1.38 | 1.38 | 1.40 | 1.46 |
| | | 0.020 | 1.90 | 0.4 | 1.73 | 1.74 | 1.75 | 1.77 | 1.81 |
| | | 0.025 | 2.40 | 0.4 | 2.10 | 2.12 | 2.12 | 2.15 | 2.18 |
| | | 0.030 | 2.80 | 0.5 | 2.48 | 2.50 | 2.51 | 2.54 | 2.57 |
| | 24.6 | 0.01 | 1.00 | 0.2 | 1.05 | 1.05 | 1.05 | 1.06 | 1.15 |
| | (110) | 0.02 | 1.75 | 0.2 | 1.73 | 1.74 | 1.75 | 1.77 | 1.81 |
| | W | 0.03 | 2.70 | 0.3 | 2.48 | 2.50 | 2.51 | 2.54 | 2.57 |
| | | 0.04 | 3.60 | 0.35 | 3.26 | 3.28 | 3.28 | 3.33 | 3.35 |
| | | 0.05 | 4.20 | 0.4 | 4.04 | 4.07 | 4.07 | 4.13 | 4.14 |
| | | 0.06 | 5.00 | 0.4 | 4.82 | 4.85 | 4.86 | 4.93 | 4.94 |
| | | 0.07 | 5.90 | 0.5 | 5.60 | 5.64 | 5.65 | 5.73 | 5.74 |
| | | 0.08 | 6.40 | 0.5 | 6.39 | 6.43 | 6.45 | 6.53 | 6.54 |
| | | 0.09 | 7.20 | 0.6 | 7.17 | 7.22 | 7.24 | 7.33 | 7.33 |
| | | 0.10 | 8.10 | 0.6 | 7.95 | 8.01 | 8.03 | 8.12 | 8.13 |
| | 50 | 0.05 | 4.2 | 1.0 | 4.04 | 4.07 | 4.07 | 4.13 | 4.14 |
| | (110) | 0.09 | 7.5 | 0.9 | 7.17 | 7.22 | 7.24 | 7.33 | 7.33 |
| | W | 0.13 | 10.1 | 0.8 | 10.29 | 10.36 | 10.38 | 10.50 | 10.50 |
| | | 0.17 | 13.6 | 0.8 | 13.35 | 13.45 | 13.47 | 13.62 | 13.61 |
| | | 0.21 | 16.6 | 0.6 | 16.34 | 16.47 | 16.49 | 16.66 | 16.65 |
| | | 0.25 | 19.5 | 0.6 | 19.25 | 19.40 | 19.43 | 19.60 | 19.58 |
| | | 0.29 | 22.5 | 0.7 | 22.07 | 22.23 | 22.27 | 22.43 | 22.41 |
| | 70 | 0.34 | 25.9 | 0.6 | 25.42 | 25.61 | 25.65 | 25.78 | 25.76 |
| | (110) | 0.43 | 31.3 | 0.4 | 30.91 | 31.14 | 31.19 | 31.22 | 31.20 |
| | W | 0.51 | 35.2 | 0.5 | 35.10 | 35.36 | 35.42 | 35.32 | 35.31 |
| | | 0.67 | 41.1 | 0.4 | 41.21 | 41.52 | 41.59 | 41.21 | 41.22 |
| | | 0.77 | 42.9 | 0.4 | 43.30 | 43.63 | 43.70 | 43.20 | 43.22 |
| | | 0.87 | 44.1 | 0.6 | 43.98 | 44.31 | 44.38 | 43.84 | 43.86 |
| | | 0.97 | 43.3 | 0.6 | 43.21 | 43.54 | 43.61 | 43.12 | 43.13 |
| [11$\bar{2}$] | 50 | 0.10 | 8.7 | 0.8 | 8.52 | 8.42 | 8.37 | 8.49 | 8.49 |
| | (110) | 0.15 | 11.9 | 0.6 | 12.67 | 12.53 | 12.45 | 12.66 | 12.63 |
| | W | 0.20 | 16.4 | 0.6 | 16.72 | 16.53 | 16.44 | 16.71 | 16.69 |
| | | 0.25 | 20.6 | 0.5 | 20.64 | 20.40 | 20.30 | 20.64 | 20.62 |

TABLE II *(continued)*

| Direction [*hkl*] | Experimental condition | $q$ (Å$^{-1}$) | $E_{obs}$ (meV) | $\Delta E$ (meV) | $E_{calc}$(meV) $N=2$ | $N=4$ | $N=5$ | $N=10$ | $N=12$ |
|---|---|---|---|---|---|---|---|---|---|
| | 70 | 0.25 | 21.2 | 0.8 | 20.64 | 20.40 | 20.30 | 20.64 | 20.62 |
| | (110) | 0.35 | 28.4 | 0.7 | 27.97 | 27.62 | 27.49 | 28.00 | 27.99 |
| | W | 0.45 | 34.5 | 0.6 | 34.42 | 33.98 | 33.84 | 34.49 | 34.47 |
| | | 0.55 | 39.8 | 0.5 | 39.86 | 39.30 | 39.18 | 39.87 | 39.85 |
| | | 0.65 | 44.0 | 0.5 | 44.14 | 43.52 | 43.41 | 44.02 | 44.00 |
| | 90 | 0.65 | 44.0 | 0.6 | 44.14 | 43.52 | 43.41 | 44.02 | 44.00 |
| | (110) | 0.75 | 47.0 | 1.0 | 47.26 | 46.60 | 46.50 | 46.91 | 46.90 |
| | W | 0.95 | 49.6 | 1.0 | 50.20 | 49.60 | 49.49 | 49.41 | 49.41 |
| [1, 1, 1.545] | 70 | 0.25 | 18.0 | 0.8 | 16.71 | 17.59 | 17.88 | 18.08 | 18.06 |
| | (110) | 0.35 | 24.8 | 0.6 | 23.03 | 24.08 | 24.40 | 24.64 | 24.62 |
| | W | 0.45 | 30.7 | 0.5 | 28.99 | 30.08 | 30.35 | 30.60 | 30.60 |
| | | 0.55 | 35.8 | 0.5 | 34.50 | 35.47 | 35.66 | 35.91 | 35.92 |
| | 90 | 0.55 | 36.0 | 0.8 | 34.50 | 35.47 | 35.66 | 35.91 | 35.92 |
| | (110), W | 0.70 | 42.6 | 0.8 | 41.75 | 42.30 | 42.33 | 42.58 | 42.61 |
| [112] | 70 | 0.15 | 11.0 | 1.2 | 10.83 | 11.19 | 11.33 | 11.48 | 11.47 |
| | (110) | 0.25 | 18.4 | 1.2 | 17.80 | 18.34 | 18.56 | 18.82 | 18.81 |
| | W | 0.35 | 26.0 | 1.2 | 24.47 | 25.07 | 25.36 | 25.73 | 25.72 |
| | | 0.45 | 32.0 | 1.2 | 30.72 | 31.25 | 31.60 | 32.07 | 32.08 |
| [1, 1, 0.0] | 90 | 0.867 | 44.0 | 0.6 | 43.98 | 44.30 | 44.38 | 43.84 | 43.86 |
| [1, 1, 0.169] | (110) | 0.874 | 44.5 | 0.6 | 44.32 | 44.61 | 44.65 | 44.13 | 44.15 |
| [1, 1, 0.309] | W | 0.894 | 45.3 | 0.6 | 45.29 | 45.48 | 45.42 | 44.97 | 44.98 |
| [1, 1, 0.425] | | 0.928 | 46.1 | 0.7 | 46.75 | 46.77 | 46.62 | 46.25 | 46.26 |
| [1, 1, 0.524] | | 0.972 | 47.7 | 0.5 | 48.53 | 48.31 | 48.12 | 47.85 | 47.85 |
| [1, 1, 0.610] | | 1.027 | 49.3 | 0.5 | 50.42 | 49.89 | 49.77 | 49.58 | 49.58 |
| [1, 1, 0.726] | | 1.133 | 52.3 | 0.5 | 53.28 | 52.18 | 52.34 | 52.25 | 52.24 |
| [1, 1, 0.821] | | 1.257 | 54.5 | 0.5 | 55.23 | 53.67 | 54.17 | 54.12 | 54.11 |
| [1, 1, 0.899] | | 1.393 | 54.7 | 0.6 | 55.84 | 54.11 | 54.74 | 54.73 | 54.72 |

sum over the $M$ observations

$$F = \frac{1}{M-N} \cdot \frac{\sum_{i=1}^{M} W_i \cdot (E_{i,\mathrm{calc}} - E_{i,\mathrm{obs}})^2}{\sum_{i=1}^{M} W_i}, \tag{7}$$

which is a measure of the goodness of the fit. $N$ is the number of fitted parameters. Calculated and observed energies at the $i^{\mathrm{th}}$ observation are

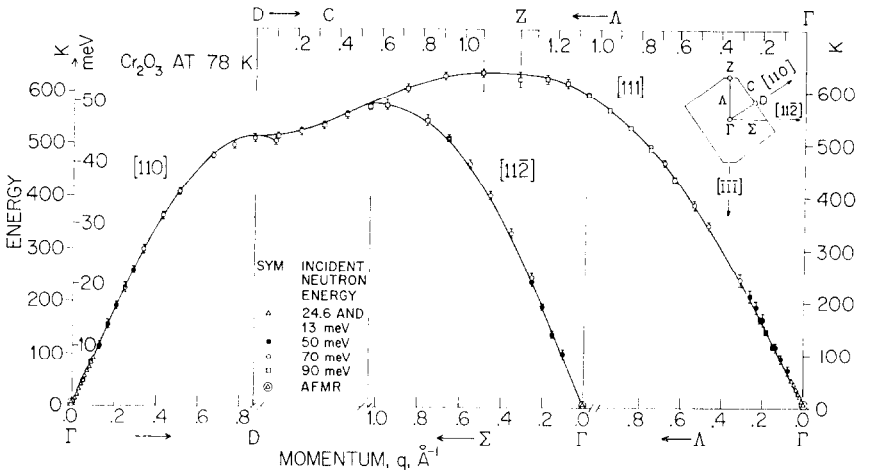


Fig. 6. The spin-wave energy dispersion relation $E(\boldsymbol{q})$ in several directions as obtained from the measurements after corrections. The curves are calculated from eq. (6) using the set of $J_m$ values labelled $N = 5$ in table III. A sketch of the B.Z. is shown in the upper right corner.

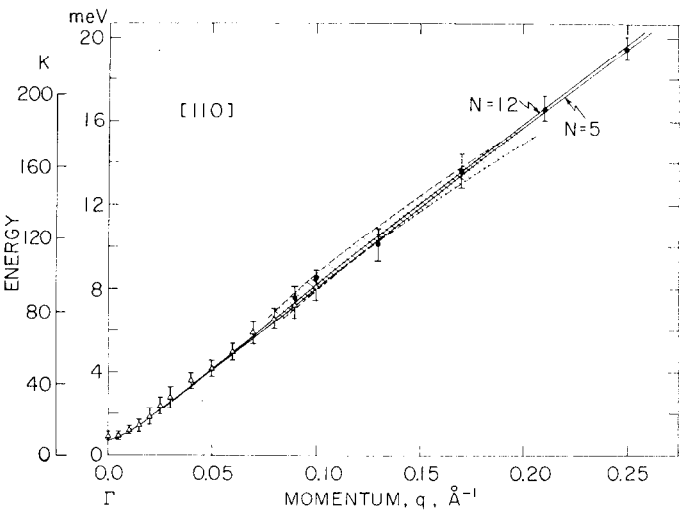


Fig. 7. A detailed picture of measured $E(\boldsymbol{q})$ along [110] for low energies compared with diffraction data[20]) (hatched region) and calculations for best fit (table III).

denoted by $E_{i,\mathrm{calc}}$ and $E_{i,\mathrm{obs}}$, respectively. The weighing function $W_i$ was taken as $1/(\Delta E_i)^2$, where $\Delta E_i$ is the estimated uncertainty of $E_{i,\mathrm{obs}}$.

The energy at $\boldsymbol{q} = 0$ was fixed at 0.68 meV (7.9 K) during the fitting procedure. The anisotropy field $H_A$ is largely determined by this value and was found to be almost independent of the number of parameters fitted.

TABLE III

Exchange interaction parameters $J_m$ in K. Values of $J_m$ for $m \leq 12$ are shown for various numbers $N$ of parameters fitted to the observed spin-wave dispersion relation at 78 K. Values of $J_1$ and $J_4$ marked by stars are correlated through the relations shown to the right. The minimum values of the function $F$(eq. (7)) is shown. For comparison, other determinations of the $J_m$'s for $Cr_2O_3$ and ruby are included.

| Number of parameters, $N$ | $J_1$ | $J_2$ | $J_3$ | $J_4$ | $J_5$ | $J_6$ | $J_7$ | $J_8$ | $J_9$ | $J_{10}$ | $F$ | |
|---|---|---|---|---|---|---|---|---|---|---|---|---|
| 2 | −94.1 | −41.1 | | | | | | | | | 1.92 | |
| 3 | −85.7 | −38.8 | −2.7 | | | | | | | | 0.523 | |
| 4 | −92.2* | −38.9 | −2.6 | −0.6* | | | | | | | 0.528 | $J_1 = -85.5 + 11.6 \cdot J_4$ |
| 5 | −87.3* | −39.6 | −0.9 | 0.2* | −2.2 | | | | | | 0.358 | $J_1 = -89.8 + 11.1 \cdot J_4$ |
| 10 | −85.6* | −37.9 | 0.0 | 0.2* | −2.2 | 0.6 | −0.3 | −1.9 | −1.8 | 2.8 | 0.223 | $J_1 = -88.1 + 10.9 \cdot J_4$ |
| 12 | −87.3* | −37.8 | 0.7 | 0.2* | −2.2 | 0.6 | −0.1 | −1.8 | −1.8 | 2.9 | 0.207 | $J_1 = -88.1 + 10.9 \cdot J_4$<br>$J_{11} = -0.0 \pm 0.3$<br>$J_{12} = 0.1 \pm 0.3$<br>$H_A = 374 \pm 14$ Oe = $= (2.98 \pm 0.11) \times 10^4$ ampere turns / m |
| Uncertainties | ±23* | ± 1.5 | ±2.0 | ±2.3* | ±0.8 | ±0.5 | ±0.5 | ±0.5 | ±0.5 | ±1.0 | | |
| Alikhanov *et al.*[19]), $Cr_2O_3$ | −86<br>±6 | −38<br>± 6 | −5.8<br>±5.8 | −2.3<br>±5.8 | | | | | | | | |
| Mollenauer and Schawlow[15]), ruby | −162 | −68.5 | −8.4 | 0.5 | | | | | | | | |
| Kisliuk *et al.*[16]) ruby | | −60 | | | | | | | | | | |

* The uncertainty of $J_1$ derives from the uncertainty of $J_4$ through the correlation.

The fitting procedure was carried through systematically by fitting from two to twelve exchange parameters $J_m$. The results are shown in table III. It was found that $J_1$ and $J_4$ could only be determined to within a linear combination, that is $F$ versus $J_4$ has a very flat minimum, and in that region $J_1$ varies linearly with $J_4$. The correlation between $J_1$ and $J_4$ can be recognised in a careful inspection of the energy expressions of appendix I. It depends upon the fact that both $J_3$ and $J_4$ are small and is under these conditions quite independent of the spin-wave propagation direction. Thus the correlation problem would not be solved by measuring in some other plane.

The inclusion of $J_5$ reduces $F$ considerably and brings a closer fit to the experimental data along [111] and along the zone boundary line C. Fig. 8 shows contours of constant $F$ for varying $J_4$ and $J_5$. The minimum is rather flat in the direction of a line satisfying $J_5 = 0.4\,J_4 - 2.2$ (in K units). The uncertainties for $J_4$ and $J_5$ as given in table III are estimated assuming $J_4$ and $J_5$ to be found within the shaded area of fig. 8.

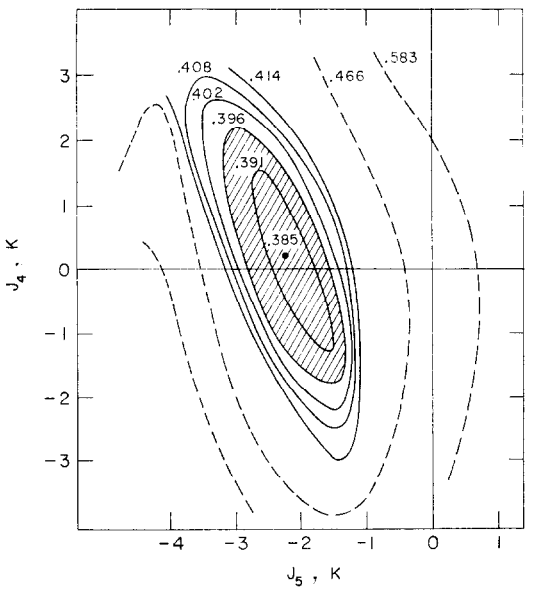


Fig. 8. Contour of constant value of $F$ (eq. (7)) in the $J_4$–$J_5$ plane. The values of $F$ for each contour are indicated. Uncertainties of $J_4$ and $J_5$ are estimated from the extension of the shaded region.

Although the discrepancies between observed and calculated energies are small at this stage of the fitting, there is still some systematic deviation in the [11$\bar{2}$] direction, and inclusion of interactions to the outer neighbours seems to be required. Regarding the smallness of the discrepancy, it may

be questionable whether this is justified. A systematic error in the measurements cannot be excluded altogether, although the source for such an error is not obvious, since the instrumental correction has already been carried out. Further, as the additional interactions will certainly come out weak, it may be argued that other interaction terms not included in the Hamiltonian, may be of equal strength. Dipolar interaction, though in first approximation contributing to the effective anisotropy field $H_A$ only, gives rise to some $\boldsymbol{q}$-dependence in $E(\boldsymbol{q})$. Similarly, anisotropic exchange (for instance in the form of pseudo-dipolar interaction) will in general contribute with some $\boldsymbol{q}$-dependence in addition to its effect on $H_A$. Despite these reservations, it is still of some interest to try and analyse the data in terms of isotropic exchange beyond the first shell of neighbours. The procedure followed was to keep 3 or 4 parameters fixed, while varying the others.

It was found that inclusion of $J_6$ and $J_7$ alone had little effect, whereas $J_8$, $J_9$ and $J_{10}$ brought about an appreciable improvement of the fit, as seen from table III. The distances corresponding to these three interactions are very close (table I), so inclusion of one of them necessarily requires inclusion of all of the three. However, the actual values of these parameters should be taken with the above-mentioned reservations. For completeness $J_{11}$ and $J_{12}$ were also included, but they were found to be vanishingly small.

The $J_m$'s in table III have not been corrected for temperature effects. However, at 78 K the spin-wave energy is reduced 1.7% from its 0 K value [20]), requiring a 1.7% higher value of the true (temperature-independent) $J$-values. Further, from Green- function theory using the RPA-approximation (section 6), a correction upwards of 8% is required because the spin value $S = \frac{3}{2}$ is to be substituted by $\langle S^z \rangle_{T=0}$, and as shown in section 6 the zero-point deviation lowers $\langle S^z \rangle_{T=0}$ to 1.38. According to Walker [26]) the RPA is a valid approximation for short-wavelength spin waves. For long-wavelength spin waves Oguchi and others [27]) using more sophisticated approaches predict that the spin-wave energy be enhanced over the spin-wave model value at $T = 0$. If an Oguchi enhancement factor is to be included in $E(\boldsymbol{q})$, the resulting $J_m$'s will of course have to be adjusted downwards.

5. *Discussion of exchange parameters.* 5.1. General remarks. Several attempts have been made to estimate theoretically the relative strengths of the four nearest-neighbour interactions in $Cr_2O_3$ [2–6]). Qualitatively, super-exchange is expected to play a role, since the Cr ions are connected by bridges of single oxygen ions (fig. 5). For $J_1$ and $J_2$ also direct cation–cation exchange may be important [4]) because direct overlap is possible between the $Cr^{3+}$–3d wave functions. Interaction between neighbours beyond the fourth can only take place through two or more intervening ions. Such indirect exchange interaction is expected to be weaker, but to show a slower

decay with increasing interionic distance than the usual superexchange interaction involving only one intermediary ion[28]).

The most striking feature of the experimentally determined $J_m$'s of table III is that $J_1$ and $J_2$ are one to two orders of magnitude stronger than $J_3$ and $J_4$. Although not directly predicted by Goodenough, this result supports his view[4]) that direct exchange may be the dominant interaction in $Cr_2O_3$. The small values of $J_3$ and $J_4$ are further compatible with his statement[29]) that they involve Cr–O–Cr angles (121° and 133° respectively) in "the range of angles within which the sign (of the superexchange interaction) changes from that of 180° to that of 90° coupling". It is interesting to notice that in $\alpha$–$Fe_2O_3$, on the contrary, $J_4$ is expected to represent a strong interaction[4]).

Another interesting feature of table III is that interactions between neighbours beyond the fourth are not all negligibly weak. Thus $J_5$ is found to be comparable in magnitude with $J_3$ and $J_4$. As $J_5$ represents an interaction between Cr ions 4.1 Å apart, direct 3d-wave-function overlap is probably very small, and the mechanism for $J_5$ is to be looked for in an indirect exchange involving two intermediary oxygen ions. To the authors' knowledge, no theoretical estimates of $J_5$ have been attempted as yet.† We hope that the data of table III will stimulate new and more detailed theoretical work on the coupling mechanisms in $Cr_2O_3$.

5.2. Comparison with existing data. For comparison, previous determinations of the exchange interactions in $Cr_2O_3$ and in ruby are included in table III. The values by Alikhanov *et al.*[19]) are derived from neutron measurements of ten points of $E(\boldsymbol{q})$ for $q < 0.51$ Å$^{-1}$ in various directions of the reciprocal space, using the diffraction technique. Regarding the limitation of their data, the agreement between their and our values of $J_1$ and $J_2$ is remarkable. (But the quoted uncertainty of $J_1$ is too optimistic). Alikhanov *et al.* did not perform a systematic study of $E(\boldsymbol{q})$, and their calculated $E(\boldsymbol{q})$ curve along [111] is much in error.

Because the structures of $Cr_2O_3$ and $\alpha$–$Al_2O_3$ (corundum) are very similar, one might expect that the magnetic interactions between $Cr^{3+}$-ion pairs would be similar in $Cr_2O_3$ and in ruby ($Cr3^+$ ions doped in $\alpha$–$Al_2O_3$). From paramagnetic resonance studies[17]) and careful interpretation of the optical spectrum[15–16]) information has indeed been obtained on these pair interactions in ruby. Mollenauer and Schawlow[15]), in their piezo-spectroscopic study, derived the value of the four nearest-neighbour interactions, included in table III. A recent determination[16]) of $J_2$ is also shown in the table. It is seen that the dominant interactions $J_1$ and $J_2$ are considerably stronger in ruby than in $Cr_2O_3$, and also $J_3$ seems to represent a stronger interaction

† But see J. B. Goodenough and J. J. Stickler, Phys. Rev. **164** (1967) 768 for ilmenites. (Note added in proof.)

in ruby. For interactions to further neighbours, Statz *et al.*[17]) claim to have detected (by EPR) interactions out to the 11th, and they indicate that those beyond the 4th are weak ($\sim$ 1 K). Incidentally, their value for $J_1$ of $-280$ K is too high.

5.3. Pair interactions in ruby and in $Cr_2O_3$. A few remarks are probably appropriate on the above differences. Because the geometries of the two near neighbour pairs are so similar[30]) in $\alpha$–$Al_2O_3$ and in $Cr_2O_3$ (table IV, two first columns) a difference of a factor of about two may at first glance seem a lot. There is good evidence, however, that the Cr ions do not substitute exactly into the Al positions in the ruby crystal. Moss and Newnham[31]) have found by $X$-ray measurements that in the mixed oxide $Al_{1\cdot92}Cr_{0\cdot08}O_3$ the interionic distance of the Cr pair along [111] is shorter than the corresponding Al pair by 0.1 Å. The pertinent data for the bonds corresponding to $J_1$ and $J_2$ are listed in table IV. For superexchange via oxygen ions, the Cr–O-distances (and the Cr–O–Cr-angles) are thought to be important, and the Cr–Cr-distance would be most decisive for a direct exchange mechanism, so that the strength of the interaction would decrease with increasing distance. Comparison between columns two and three of table IV would thus suggest the ruby interactions to be the stronger.

TABLE IV

Interatomic distances and angles related to the nearest ($J_1$) and next nearest ($J_2$) neighbour interactions. The values for "ruby" are those for $Al_{1.92}Cr_{0.08}O_3$, assuming all $Cr^{3+}$ ions to enter equivalent positions, and assuming the $O^{2-}$-lattice be that of $\alpha$–$Al_2O_3$.

| | | | ($\alpha$–$Al_2O_3$[30]) | $Cr_2O_3$[30]) | Ruby[31]) |
|---|---|---|---|---|---|
| $J_1$ | Cr–Cr | (Å) | (2.65) | 2.65 | 2.55 |
| | Cr–O | (Å) | (1.97) | 2.02 | 1.94 |
| | Cr–O–Cr | (°) | (84.6) | 82.3 | |
| $J_2$ | Cr–Cr | (Å) | (2.79) | 2.89 | 2.78 |
| | Cr–O (1) | (Å) | (1.97) | 2.02 | 1.94 |
| | O–Cr (2) | (Å) | (1.86) | 1.97 | 1.88 |
| | Cr–O–Cr | (°) | (93.6) | 93.1 | |

It is interesting to compare these observations with hydrostatic-pressure data. The body diagonal $c_H$ as well as the basal-plane dimension, $a_H$ in $Cr_2O_3$ decrease by application of hydrostatic pressure[32]). On the other hand, application of pressure is known to decrease the Néel temperature $T_N$[33]) and thus the strongest interactions $J_1$ and $J_2$. A consequence of our explanation of the stronger ruby interactions in terms of shorter interionic distances is therefore that the Cr(1)–Cr(2) distance (fig. 5) must increase

upon application of hydrostatic pressure, despite the decrease in $c_H$. This is in fact plausible, since an increased Cr(1)–Cr(2) distance involves pushing the Cr ions towards the "empty" regions of the corundum lattice. A careful high-pressure structure analysis of $Cr_2O_3$ would settle this point.

Another striking difference between ruby and $Cr_2O_3$ is the strength of the anisotropy field $H_A$. The value 374 Oe ($3.0 \times 10^4$ ampere turns/m) for $Cr_2O_3$ of table III is determined essentially from the AFMR data for $\boldsymbol{q} = 0$, and is therefore in agreement with Foner's data[9]) (350 Oe; the value 700 Oe given in ref. 9 is too high by a factor of two [11])). Artman *et al.*[11]) found that around half of this value is accounted for by classical dipolar interactions, and they attribute the second half to crystalline (or single ion) anisotropy. The latter amounts only to about 1/20 of the crystalline anisotropy found for $Cr^{3+}$ in ruby, and the explanation for that effect is also sought in eventual changes of the local geometry around $Cr^{3+}$ ions in ruby. Artman and Murphy[34]) calculate, however, that the $Cr^{3+}$ ions must be pushed in the opposite direction to that which the $X$-ray work of Moss and Newnham[31]) indicates.

6. *Thermomagnetic properties and density of states.* 6.1. Sublattice magnetization. The sublattice magnetization of an antiferromagnet describes the temperature dependence of the average value of the $z$ component of the atomic spins, $\langle S^z \rangle$. The spin-wave theory furnishes in general a good description of $\langle S^z \rangle$ at low temperatures[26]), and by application of the Green-function technique $\langle S^z \rangle$ may be calculated quite accurately for all temperatures right up to the Néel point. One interesting prediction of the spin-wave theory is the "zeropoint deviation" of $\langle S^z \rangle$, that is, that $\langle S^z \rangle$ will not reach the full value of $S$ even at $T = 0$. The origin of the zeropoint deviation is found in the fact that the collinear spin state of an antiferromagnet is not the proper ground state of the Heisenberg Hamiltonian eq. (5). The magnitude of the zeropoint deviation is still unclear, as fully unambiguous measurements are difficult to carry out. For $Cr_2O_3$ the magnetic moment associated with each $Cr^{3+}$ was measured by neutron diffraction[35]) to be $(2.76 \pm 0.03)\ \mu_B$ at 4.2 K. Using $g = 1.97$[9]) this gives $\langle S^z \rangle_{T=0} = 1.40 \pm 0.015$. This 7% deviation from the spin-only value of 1.5 also includes, however, a spin deficit due to covalency. The covalent character in the $Cr^{3+}$–$O^{2-}$ bonds involves a small spin transfer from the $Cr^{3+}$–3d wave function into the $O^{2-}$–2p wave functions and this transferred spin is not observable in conventional neutron diffraction. The covalency is intimately connected to the strength of the superexchange interaction via the $O^{2-}$ ions[36]). For typical cases in cubic crystals, the effect may amount to several per cent.

Application of Green-function theory to derive temperature-dependent properties, such as the sublattice magnetization, always involves an ap-

proximation at some stage in order to decouple a set of coupled Green functions. The simplest decoupling procedure one can use is equivalent to assuming random phases between the $z$ components and the $x$ or $y$ components of the spin in the calculation of expectation values. The random-phase approximation (RPA) involves therefore the following type of substitutions[37])

$$\langle S^z S^+ S^- \rangle \rightarrow \langle S^z \rangle \langle S^+ S^- \rangle. \tag{8}$$

It represents a "molecular field theory of second order" applied to the spin-wave theory. The RPA has the definite advantage over more elaborate decoupling procedures that it can easily be applied to any crystal lattice and to any number of interaction parameters. A general prediction of the RPA is that the spin value $S$ entering the spin-wave energy $E(\boldsymbol{q})$ for an antiferromagnet is to be substituted by $\langle S^z \rangle$, so that the temperature dependence of $E(\boldsymbol{q})$ follows that of the sublattice magnetization[37]). This has been found to be a good description of the situation in $Cr_2O_3$[20]).

We have calculated the temperature dependence of $\langle S^z \rangle$ using the observed spin-wave data in conjunction with the RPA as developed by Mills *et al.*[37]) The calculation involves the evaluation of a spin-wave occupation number $\Phi_j$ associated with sublattice $j$. In the absence of an external magnetic field $\Phi_j = \Phi$ is the same for all sublattices. For $Cr_2O_3$ one finds

$$\Phi = \frac{1}{2N_c} \sum_{\boldsymbol{q}} \left[ \frac{(A + C)}{E_{T=0}(\boldsymbol{q})} \cdot \frac{\sinh(X(\boldsymbol{q}, T))}{\cosh(X(\boldsymbol{q}, T)) - 1} - 1 \right], \tag{9}$$

where

$$X(\boldsymbol{q}, T) = P(T) \cdot E_{T=0}(\boldsymbol{q}) \tag{10}$$

and

$$P(T) = \frac{\langle S^z \rangle}{\langle S^z \rangle_{T=0}} \cdot \frac{1}{k_B T}. \tag{11}$$

The sublattice magnetization is then given by[37])

$$\langle S^z \rangle = S - \Phi + \frac{(2S + 1) \cdot \Phi^{2S+1}}{(1 + \Phi)^{2S+1} - \Phi^{2S+1}}, \tag{12}$$

$k_B$ is the Boltzmann constant, $S$ is the spin value and $N_c$ is the number of unit cells. The summation of eq. (9) was performed numerically.

The sum is determined mainly by the spin-wave spectrum $E(\boldsymbol{q})$ rather than by individual sets of $J_m$ values. Therefore the $\langle S^z \rangle$ calculated is only slightly dependent upon the actual choice of the set of $J_m$ of table III. In performing the summation the smaller B.Z. of the $\alpha$–$Fe_2O_3$ type spin structure[22]) was used, and $E(\boldsymbol{q})$ was properly "folded over" to give formally an acoustical and an optical branch in this reduced zone scheme. By further restricting the summation to the irreducible (1/12) part of the B.Z. volume, the computer labour was greatly reduced. The irreducible volume element

was divided up into $n$ equals cells, with $n$ ranging up to 30164 and the contributions from all cells were added. Convergence was checked by varying $n$. The summed volume of the $n$ cells came out within 0.07% of the correct 1/12 B.Z. volume.

A set of values of $P(T)$ ranging from 5 to $10^{-5}$ was chosen, and the summation of eq. (9) was performed for each. For each $\Phi$ obtained, $\langle S^z \rangle$ was calculated from eq. (12), and finally the temperatures to which the actual $P(T)$ corresponded were solved from eq. (11). The $\langle S^z \rangle$ so obtained is shown in fig. 9. It is in particular noticed that $\langle S^z \rangle_{T=0}$ takes on a value 8.0% lower than 1.5. This represents the "zeropoint spin deviation". For comparison, the deviation is calculated to be 5.0%[10]) in a b.c.c. antiferromagnet of spin $\frac{3}{2}$ and with nearest-neighbour interaction only. The anisotropy field $H_A$ would reduce the deviation only slightly.

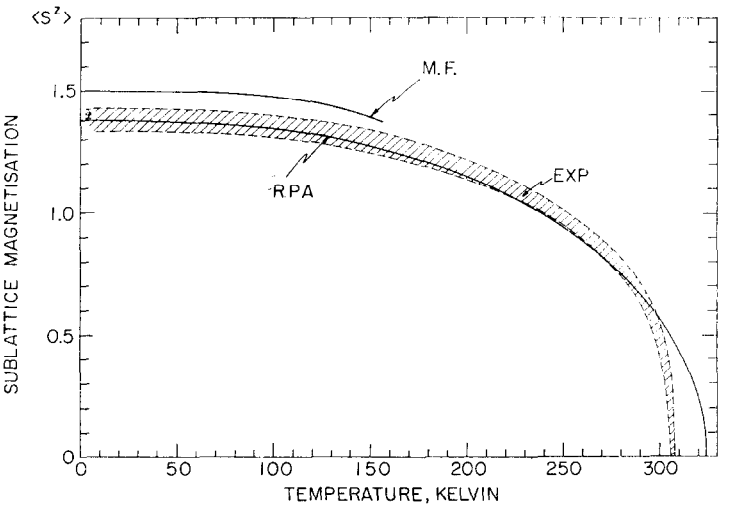


Fig. 9. The sublattice magnetization $\langle S^z \rangle$ versus temperature as measured (one point and hatched region) and as calculated using the random phase approximation (RPA) and the molecular-field theory (M. F.).

Fig. 9 compares the calculated $\langle S^z \rangle$ with experiments.The temperature variation of the sublattice magnetization has been measured by means of neutron diffraction by several workers[38]). We have made a composite curve of their results and normalised it to 1.38 at $T = 0$. The hatched region contains the scattering of points within each of the three sources as well as some minor discrepancies between the three measurements. Sublattice magnetization calculated from the parallel susceptibility also falls inside the hatched region[38c]).

The overall agreement between measured and calculated $\langle S^z \rangle$ is good, although there are significant discrepancies in the details. The experimental curve seems to decrease slower with increasing temperature than the calculated one up to a certain point, beyond which the experimental curve shows an anomalously sharp drop to zero. The sharp drop might possibly suggest some admixture of first order character into the transition at 308 K. Such a view is supported by the observation that the lattice parameters of $Cr_2O_3$ change quite abruptly near $T_N$[39]). In particular, the body diagonal $c_H$ is contracted slightly on heating through $T_N$. Furthermore, hydrostatic pressure is known on the one hand to decrease $c_H$[32]), on the other hand, to have the surprising effect of lowering $T_N$[33]). It therefore seems that the intrinsic magnetostriction of $Cr_2O_3$ is strong enough to alter the lattice parameters so much that the spin structure collapses prematurely through a cooperative effect. This could be so if a small contraction of $c_H$, say, was sufficient to lower $|J_1|$ appreciably, as the pressure data[33]) may indicate. As discussed in the previous section, this mechanism requires that the Cr(1)–Cr(2) distance increase despite a decrease in $c_H$, thus reducing the overlap between the $Cr^{3+}$–3d wave functions (assuming direct exchange dominant). The sharper increase with temperature of the lattice parameter

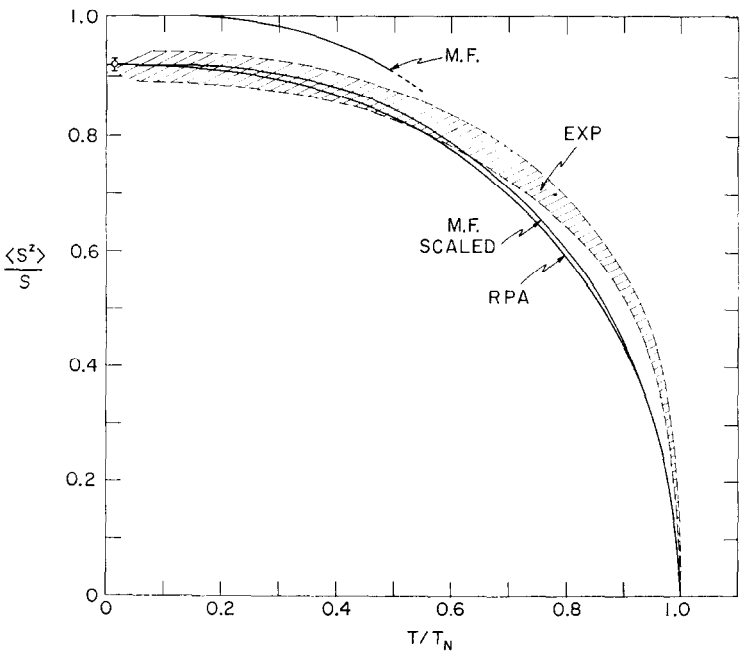


Fig. 10. Sublattice magnetization versus temperature shown on a reduced scale. For comparison the molecular-field curve (M. F.) has been scaled to the random phase approximation (RPA) curve at $T = 0$.

$a_H$ (normal to $c_H$) near $T_N$[39]) would probably have a similar weakening effect on $J_2$.

Fig. 10 shows the calculated sublattice magnetization $\langle S^z \rangle$ plotted on a reduced scale. It is noticed that the RPA calculation agrees in most of the temperature range with the molecular field (M. F.) calculations for $S = \frac{3}{2}$ (also shown) when the two curves are normalised to each other at $T = 0$. The molecular field theory does not predict any zeropoint deviation, and the temperature variation at low $T$ is less for M.F. than for RPA, because the M.F. does not include any spin-wave effects as does RPA. It should be noticed, however, that since the spin-wave spectrum has a gap of 7.9 K, the $T^2$ dependence of $\langle S^z \rangle$ is not expected to hold for $T \gtrsim 8$–10 K.

6.2. The Néel point $T_N$. $T_N$ may be obtained either as the extrapolated temperature as $P(T) \to 0$, or a closed expression may be obtained from eqs. (9)–(12) through proper expansions for $\langle S^z \rangle$ small and $\Phi$ large[22]):

$$T_N = \frac{S(S+1)}{3k_B} \cdot \left[ \frac{\langle S^z \rangle_{T=0}}{N_c} \sum_{q} \frac{A + C}{|E_{T=0}(q)|^2} \right]^{-1}. \tag{13}$$

In either case one obtains the same result. Because $E(q)$ is measured at 78 K, the $J_m$ as given in table III should be adjusted upwards by 1.7%, which is the amount the $\langle S^z \rangle$ and also $E(q)$ changes from $T = 0$ to $T = 78$ K. Doing so and performing the summation, one finds $T_N = (324 \pm 3)$ K. The uncertainty covers the variation of $T_N$ with the various sets of $J_m$'s of table III as well as the variation due to taking $H_A = 0$ or finite.

This result is to be contrasted with the prediction of the molecular field theory (M.F.)[40]):

$$T_N = \frac{2S(S+1)}{3k_B} \sum_{m} \varepsilon_m Z_m J_m. \tag{14}$$

$Z_m$ is the number of neighbours of type $m$, and $\varepsilon_m$ takes on the value $+1$ for pairs of same spins and $-1$ for pairs of opposite spins. Using eq. (14) we get $T_N = 523 \pm 39$ K. It is well known[40]), however, that the M. F. predicts too high values of $T_N$. Consequently any evaluation of the exchange constants from $T_N$ using M.F. is unreliable.

There are many other effective field theories available that are considered to give $T_N$ more accurately than M.F. (Oguchi, constant-coupling, Bethe–Peierls–Weiss, high-temperature expansion). These are, however, usually developed for cubic crystal symmetries and for one nearest-neighbour interaction $J$ only, and are thus not directly applicable to our case. Extensions of the Green-function calculation beyond the RPA have been made, but these also are valid for simple cases only, and it is doubtful whether they indeed represent improvements over the RPA. Thus the Callen decoupling method[10]) as well as that of Oguchi[27]) do not predict a temperature de-

pendence of $E(\boldsymbol{q})$ for $Cr_2O_3$ as well in agreement with experiments as the RPA[20]).

6.3. Curie-Weiss temperature $\theta$ and perpendicular susceptibility $\chi_\perp$. The paramagnetic Curie point $\theta$ (the Curie–Weiss temperature) and the perpendicular susceptibility below $T_N$ are known to be well described in terms of $J_m$'s within the molecular field theory[40]). $\theta$ for $Cr_2O_3$ is experimentally determined to be 550 ± 50 K from high-temperature susceptibility data by Foëx and Graff[41]). Other values, ranging from 480 K to 1070 K are also found in the literature. Using the M.F. formula[40])

$$\theta = \frac{2S(S+1)}{3k_B} \left| \sum_m Z_m \cdot J_m \right|, \tag{15}$$

we calculate $\theta = 527 \pm 76$ K with the set of $J_m$'s from the five-parameter fit and $\theta = 502 \pm 75$ K with the set from the ten-parameter fit. The perpendicular susceptibility $\chi_\perp$ is constant below $T_N$ in the M.F. and is expressed by[40])

$$\chi_\perp = \frac{N_v g^2 \mu_B^2}{2 \cdot \sum_m (\varepsilon_m - 1) Z_m \cdot J_m}. \tag{16}$$

$N_v$ is the number of magnetic ions per unit volume. Using 5.21 g/cm$^3$ for the density of $Cr_2O_3$, $96 \times 10^{-24}$ cm$^3$ for the volume of the unit cell, and $g = 1.97$, we find $\chi_\perp = 22.9 \pm 2.6$ from the 5-parameter data, ($N = 5$), and $\chi_\perp = 23.8 \pm 2.6$ from the 10 parameter fit ($N = 10$), both in units of $10^{-6}$ erg/(gauss)$^2$g. These may be compared to Foner's[9]) measured value 22.4 ± 0.4 (same unit) at 4.2 K. Here, as for $\theta$, most of the calculated uncertainty arises from the $J_1$–$J_4$ correlation.

6.4. Density of states $\rho(E)$. The density of states $\rho(E)$ for spin waves in $Cr_2O_3$ at 78 K is shown in fig. 11. The calculation of $\rho(E)$ was performed by a simple sampling of the energies, falling within groups of widths 11.6 K, at 30164 different wave vectors in the irreducible unit of the Brillouin zone. The theoretical expression for $E(\boldsymbol{q})$ was used with the $J_m$ values of table III. Again, the result is only slightly dependent upon the choice of the set of $J_m$'s, since each set parameterises the observed $E(\boldsymbol{q})$.

The two distinct critical points are due to the saddle points in $E(\boldsymbol{q})$ at ($\frac{1}{2}$ $\frac{1}{2}$ 0) and ($\frac{1}{2}$ $\frac{1}{2}$ 1), respectively. That originating from the saddle point at (1 1 1) is not resolved.

The density of states $\rho(E)$ is of interest in connection with the spectroscopy of "magnon-exciton" and "two-magnon" processes. The optical sidebands, the infrared absorption band, and the optical Raman scattering from antiferromagnets are all determined by modified density of state functions[42]).

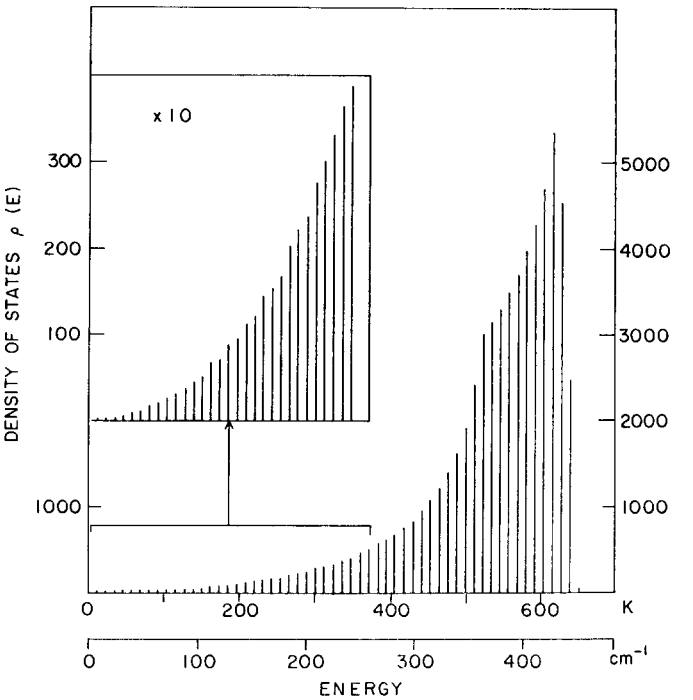


Fig. 11. Density of spin-wave states $\rho(E)$ at 78 K calculated from the theoretical $E(\boldsymbol{q})$ using the experimental $J_m$ labeled $N = 5$ in table III.

7. *Conclusion.* In this paper we have reported a detailed study of the spin-wave dispersion relation in $Cr_2O_3$ at 78 K by means of inelastic neutron scattering. The neutron data have been corrected for instrumental resolution effects by a careful computer analysis of all aspects of the resolution properties of the triple-axis spectrometer. The corrections are important, in particular, in the low-energy end of the spectrum, where they amounted to as much as 0.9 meV for extreme cases.

The experimental dispersion relation can be fitted by a theoretical function based on a Heisenberg spin Hamiltonian involving an effective anisotropy field $H_A$ and exchange interactions $J_m$ to the near neighbours. Only the exchange interactions between first ($J_1$) and second ($J_2$) nearest neighbours are found to be strong, but the data could not be fitted by the two interactions alone. Some difficulties were encountered in interpreting the data in terms of more than 3 nearest-neighbour interactions, as $J_1$ and $J_4$ were strongly correlated (table III). The strength and sign of $J_4$ is thus uncertain, although it is definitely weak compared to $J_1$ and $J_2$. $J_3$ is weak and probably negative, as is $J_5$. The fit with 5 parameters is acceptable though not perfect. Inclusion of further neighbour interactions $J_6$ and $J_7$ had no effect, whereas small negative values of $J_8$ and $J_9$ and a small positive $J_{10}$ improved the fit.

$J_{11}$ and $J_{12}$ were also included for completeness, but came out very small. The distance to the 10th nearest neighbour is 5.8 Å. The $\boldsymbol{q}$-dependence of the dipolar and possible pseudo-dipolar interaction has not been considered in the interpretation of the data.

The values of $J_1$ and $J_2$ found through the present work are only 55–65% of the corresponding interactions found by optical methods between $Cr^{3+}$-ions in ruby. A possible reason for the difference is briefly discussed.

Using the $J_m$ values of table III, we have calculated the sublattice magnetization $\langle S^z \rangle$, the Néel point $T_N$, the Curie–Weiss temperature $\theta$, and the perpendicular susceptibility $\chi_\perp$. $\langle S^z \rangle$ and $T_N$ were calculated using Green-function theory in the random-phase approximation and were found to agree well with experiments. At zero temperature we calculate $\langle S^z \rangle_{T=0} = 1.38$, compared with 1.40 observed, and 1.50 expected if neither zeropoint spin-wave deviation nor covalency effects were present. The calculated $T_N$ is $324 \pm 3$ K, slightly above the experimental 308 K. $\theta$ and $\chi_\perp$ were found from molecular field theory calculations: $\theta$(calc) $= 515 \pm 88$ K compared to $\theta$(obs) $= 550 \pm 50$ K, and $\chi_\perp$ (calc) $= 23.3 \pm 3.0$ compared to $\chi_\perp$ (obs) $= 22.4 \pm 0.4$, in units of $10^{-6}$ erg/(gauss)$^2$·g.

We feel that the generally good agreement found between measured properties and those calculated from our spin-wave data justifies a conclusion that a unified description of the magnetism in $Cr_2O_3$ in terms of exchange interaction parameters has now been found. However, the problem of how to derive these quantities from first principles still remains unsolved. We also conclude that the random-phase approximation offers a good, although not complete, description of the temperature dependence of the sublattice magnetization, as it does for the spin-wave energy.

Acknowledgments. One of us (EJS) is grateful for a fellowship from Norges teknisk-naturvitenskapelige forskningsråd, Oslo. The loan of a single crystal of $Cr_2O_3$ from W. S. Brower, Jr., National Bureau of Standards, Washington, D. C. is sincerely acknowledged.

## APPENDIX I

The spin-wave energy dispersion relation for $Cr_2O_3$ is of the form[22]

$$E(\boldsymbol{q}) = [(A + C)^2 - (BB^* + DD^* + BD^* + B^*D)]^{\frac{1}{2}}.$$

When an anisotropy field $H_A$ and 12 nearest-neighbour exchange interactions as listed in table I are involved, the functions are

$$A = \mu_B g H_A + 2S(-J_1 - 3J_2 - 3J_3 + 6J_4 - J_5 + (6 - 2W_c)\cdot J_6 + (6 - 2V_c)\cdot J_7 - 6J_8 - 3J_9 - 3J_{10} - 3J_{11} + 6J_{12}),$$

$$BB^* = 4S^2(R^2 + J_3^2 \cdot M_c + 2R \cdot J_3 \cdot V_c + J_{11} \cdot (J_{11} \cdot M_{2c} + \\ + 2R \cdot U_{2c} + 2J_3 \cdot (2W_c + Q_c)),$$

$$C = -4S(J_4 \cdot U_c + J_{12} \cdot Y_c),$$

$$DD^* = 4S^2[(J_2^2 + J_9^2)\, M_c + J_5^2 + J_{10}^2 \cdot M_{2c} + \\ + 2J_5 \cdot (J_2 \cdot V_c + J_9 \cdot W_{pc} + J_{10} \cdot U_{2c}) + \\ + 2J_2 \cdot (J_9(2V_c + U_{2c}) + J_{10} \cdot (2W_c + Q_c)) + \\ + 2J_9 \cdot J_{10}(V_c + 2S_c)],$$

$$BD^* + B^*D = 8S^2[R((J_2 + J_9) \cdot U_c + J_5 \cdot Z_c + J_{10} \cdot Y_c) + \\ + J_3(J_2 \cdot (Y_c + 2U_c) + J_5 \cdot U_c + J_9 \cdot Z_c \cdot M_c + J_{10} \cdot (U_c + 2S_{2c})) + \\ + J_{11}(J_2(U_c + 2S_{2c}) + J_5 \cdot Y_c + J_9 \cdot (Z_c(Q_c + 2W_c) - Y_c) + \\ + J_{10}(2Y_c + S_{3c}))],$$

where the geometrical functions are defined as follows in terms of the three rhombohedral lattice vectors $\boldsymbol{t}_1$, $\boldsymbol{t}_2$ and $\boldsymbol{t}_3$ and the spin-wave wave vector $\boldsymbol{q}$:

$$U_c = \cos \boldsymbol{q}/2 \cdot (\boldsymbol{t}_1 + \boldsymbol{t}_2 - \boldsymbol{t}_3) + \cos \boldsymbol{q}/2 \cdot (\boldsymbol{t}_2 + \boldsymbol{t}_3 - \boldsymbol{t}_1) + \\ + \cos \boldsymbol{q}/2 \cdot (\boldsymbol{t}_3 + \boldsymbol{t}_1 - \boldsymbol{t}_2),$$

$U_{2c}$ same form as $U_c$, but $\boldsymbol{q} \to 2\boldsymbol{q}$,

$$V_c = \cos \boldsymbol{q} \cdot \boldsymbol{t}_1 + \cos \boldsymbol{q} \cdot \boldsymbol{t}_2 + \cos \boldsymbol{q} \cdot \boldsymbol{t}_3,$$

$$W_c = \cos \boldsymbol{q} \cdot (\boldsymbol{t}_1 - \boldsymbol{t}_2) + \cos \boldsymbol{q} \cdot (\boldsymbol{t}_2 - \boldsymbol{t}_3) + \cos \boldsymbol{q} \cdot (\boldsymbol{t}_3 - \boldsymbol{t}_1),$$

$W_{2c}$, same form as $W_c$, but $\boldsymbol{q} \to 2\boldsymbol{q}$,

$W_{pc}$, same form as $W_c$, but sums instead of differences,

$$Y_c = \cos \boldsymbol{q}/2 \cdot (3\boldsymbol{t}_1 - \boldsymbol{t}_2 - \boldsymbol{t}_3) + \cos \boldsymbol{q}/2 \cdot (3\boldsymbol{t}_2 - \boldsymbol{t}_3 - \boldsymbol{t}_1) + \\ + \cos \boldsymbol{q}/2 \cdot (3\boldsymbol{t}_3 - \boldsymbol{t}_1 - \boldsymbol{t}_2),$$

$$Z_c = \cos \boldsymbol{q}/2 \cdot (\boldsymbol{t}_1 + \boldsymbol{t}_2 + \boldsymbol{t}_3),$$

$$Q_c = \cos \boldsymbol{q} \cdot (2\boldsymbol{t}_1 - \boldsymbol{t}_2 - \boldsymbol{t}_3) + \cos \boldsymbol{q} \cdot (2\boldsymbol{t}_2 - \boldsymbol{t}_3 - \boldsymbol{t}_1) + \\ + \cos \boldsymbol{q} \cdot (2\boldsymbol{t}_3 - \boldsymbol{t}_1 - \boldsymbol{t}_2),$$

$$S_c = \cos(\tfrac{3}{2}\boldsymbol{q} \cdot (\boldsymbol{t}_1 - \boldsymbol{t}_2)) \cos \boldsymbol{q}/2 \cdot (\boldsymbol{t}_1 + \boldsymbol{t}_2) + \\ + \cos(\tfrac{3}{2}\boldsymbol{q} \cdot (\boldsymbol{t}_2 - \boldsymbol{t}_3)) \cos \boldsymbol{q}/2 \cdot (\boldsymbol{t}_2 + \boldsymbol{t}_3) + \\ + \cos(\tfrac{3}{2}\boldsymbol{q} \cdot (\boldsymbol{t}_3 - \boldsymbol{t}_1)) \cos \boldsymbol{q}/2 \cdot (\boldsymbol{t}_3 + \boldsymbol{t}_1),$$

$$S_{2c} = \cos(\boldsymbol{q}/2 \cdot \boldsymbol{t}_1) \cdot \cos \tfrac{3}{2}\boldsymbol{q} \cdot (\boldsymbol{t}_2 - \boldsymbol{t}_3) + \cos(\boldsymbol{q}/2 \cdot \boldsymbol{t}_2) \cos \tfrac{3}{2}\boldsymbol{q} \cdot (\boldsymbol{t}_3 - \boldsymbol{t}_1) + \\ + \cos(\boldsymbol{q}/2 \cdot \boldsymbol{t}_3) \cos \tfrac{3}{2}\boldsymbol{q} \cdot (\boldsymbol{t}_1 - \boldsymbol{t}_2),$$

$$S_{3c} = \cos \boldsymbol{q}/2\cdot(5\boldsymbol{t}_1 - 3(\boldsymbol{t}_2 + \boldsymbol{t}_3)) + \cos \boldsymbol{q}/2\cdot(5\boldsymbol{t}_2 - 3(\boldsymbol{t}_3 + \boldsymbol{t}_1)) + \\ + \cos \boldsymbol{q}/2\cdot(5\boldsymbol{t}_3 - 3(\boldsymbol{t}_1 + \boldsymbol{t}_2)).$$

$$M_c = 3 + 2\cdot W_c,$$

$$M_{2c} = 3 + 2\cdot W_{2c},$$

and

$$R = J_1 + 2\cdot J_8\cdot W_c.$$

## REFERENCES


1) Brockhouse, B. N., J. chem. Phys. **21** (1953) 961.
2) Li, Y. Y., Phys. Rev. **102** (1956) 1051.
3) Iida, S., J. Phys. Soc. Japan **11** (1956) 1300.
4) Goodenough, J. B., Phys. Rev. **117** (1960) 1442.
5) Osmond, W. P., Proc. Phys. Soc. **79** (1962) 394.
6) Halpern, V., Proc. Roy. Soc. **A291** (1966) 113.
7) Cox, D. E., Takei, W. J. and Shirane, G., J. Phys. Chem. Solids **24** (1963) 405.
8) Bertaut, E. F., Proc. of Int. Congr. on Magnetism, Nottingham 1964, 516.
9) Foner, S., Phys. Rev. **130** (1963) 183.
10) Anderson, F. B. and Callen, H. B., Phys. Rev. **136** (1964) A 1068.
11) Artman, J. O., Murphy, J. C. and Foner, S., J. appl. Phys. **36** (1965) 986.
12) Silverstein, S. D. and Jacobs, I. S., Phys. Rev. Letters **12** (1964) 670.
13) McClure, D. S., J. Phys. Chem. Solids **3** (1957) 311.
Wickersheim, K. A., J. appl. Phys. **34** (1963) 1224.
Stager, C. V., J. appl. Phys. **34** (1963) 1232.
van der Ziel, J. P., Phys. Rev. **161** (1967) 483.
14) Pratt, G. W. and Bailey, P. T., Phys. Rev. **131** (1963) 1923.
Allen, J. W., Macfarlane, R. M. and White, R. L., Phys. Rev. **179** (1969) 523.
15) Mollenauer, L. F. and Schawlow, A. L., Phys. Rev. **168** (1968) 309.
16) Kisliuk, P., Chang, N. C., Scott, P. L. and Pryce, M. H. L., Phys. Rev. **184** (1969) 367.
17) Statz, H., Rimai, L., Weber, M. J., deMars, G. A. and Koster, G. F., J. appl. Phys. **32** (1967) 218S.
18) Samuelsen, E. J., Phys. Letters **26A** (1968) 160.
19) Alikhanov, R. A., Dimitrijevic, Z., Kowalska, A., Krasnicki, S., Rzany, H., Todorovic, J. and Wanic, A., Phys. Status solidi **32** (1969) 41.
20) Samuelsen, E. J., Physica **45** (1969) 12.
21) Samuelsen, E. J., Hutchings, M. T. and Shirane, G., Bull. Amer. Phys. Soc. **14** (1969) 539, and Solid State Commun. **7** (1969) 1043.
22) Samuelsen, E. J., Physica **43** (1969) 353.
23) Cooper, M. J. and Nathans, R., Acta cryst. **23** (1967) 357.
24) See for instance Collins, M. F., Minkiewicz, V. J., Nathans, R., Passell, L. and Shirane, G., Phys. Rev. **179** (1969) 417.
25) Powell, M. J. D., The Computer Journal **7** (1965) 303.
26) Walker, L. R., Magnetism I, edited by Rado and Suhl, Academic Press, London, New York (1963).
27) Oguchi, T., Phys. Rev. **117** (1960) 117.

Anderson, B. F. and Callen, H. F., ref. 10.
Liu, S. H., Phys. Rev. **142** (1966) 267.
28) Anderson, P. W., Phys. Rev. **115** (1959) 2.
29) Goodenough, J. B., Magnetism and the Chemical Bond, Interscience (1963) 244.
30) Newnham, R. E. and de Haan, Y. M., Z. Krist. **117** (1962) 235.
31) Moss, S. C. and Newnham, R. E., Z. Krist. **120** (1964) 359.
32) Lewis Jr., G. K., and Drickamer, H. G., J. chem. Phys. **45** (1966) 224.
33) Worlton, T. G., Brugger, R. M. and Bermion, R. B., J. Phys. Chem. Solids **29** (1968) 435.
34) Artman, J. O. and Murphy, J. C., Phys. Rev. **135** (1964) A 1622.
35) Corliss, L. M., Hastings, J. M., Nathans, R. and Shirane, G., J. appl. Phys. **36** (1965) 1099.
36) See for instance Owen, J. and Thornley, J. H. M., Reports on Progress in Physics **XXIX** (1966) 675.
37) Mills, R. E., Kenan, R. P. and Milford, F. J., Phys. Rev. **145** (1966) 704.
38) a) Corliss, L. M. and Hastings, J. M., J. Physique **25** (1964) 557.
b) Møglestue, K. T., Thesis, Oslo University (1965).
c) Shaked, H. and Shtrikman, S., Solid State Commun. **6** (1968) 425.
39) Greenwald, S., Nature **177** (1956) 286.
40) Smart, S., Effective Field Theories of Magnetism, Saunders, Philadelphia and London (1966).
41) Foëx, G. and Graff, M., CR Acad. Sci. **209** (1939) 160.
42) Loudon, R., Advances in Phys. **17** (1968) 243.